Computational Modelling of Concrete Structures – Bićanić et al. (Eds)
© 2014 Taylor & Francis Group, London, ISBN 978-1-138-00145-9

Multi-scale (FE^2) analysis of material failure in cement/ aggregate-type composite structures

J. Oliver, M. Caicedo, E. Roubin & J.A. Hernández
Technical University of Catalonia (UPC), Barcelona, Spain
International Center for Numerical Methods in Engineering (CIMNE), Barcelona, Spain

A. Huespe
CIMEC-Universidad del Litoral (UNL), Santa Fe, Argentina

ABSTRACT: The work proposes a FE^2 multiscale approach to computational modeling of material failure in concrete-like structures, made of cement/aggregate-type composite materials. Keeping the approach in a classical homogenization setting, a multiscale model is proposed, which naturally provides a microscopic length-scale to be exported to the macrostructure. There, this length scale is used as regularization parameter in the context of the Continuum Strong Discontinuity Approach to material failure, and finite elements with embedded strong discontinuities (E-FEM). The resulting technique allows robust modeling of crack propagation at the structural scale, accounting for the mesostructure morphology, supplies proper energy dissipation and solutions independent of the finite element and RVE sizes. Application to a number of examples, in the range from light-aggregate concrete to regular concrete, shows the potentiality of the method.

1 INTRODUCTION

Two-scale computational modeling of materials is a subject of increasing interest in computational mechanics. When dealing with materials displaying a spatially smooth behavior there is wide consensus, and some suitable mechanical approaches to the problem are available in the literature. For instance, the so-called *FE^2 methods*, based on the hierarchical, bottom-up one-way coupled, description of the material using the finite element method in both scales, and computational homogenization procedures at the low scale, is nowadays one of the most popular approaches. At the heart of the direct computational homogenization procedure lies the notion of Representative Volume Element (RVE) defined as the smallest possible region representative of the whole heterogeneous media on average.

Alternatively, two-scale computational modeling for *material failure analysis* is more controversial, and exhibits additional complexity. Either if *discrete approaches* (based on non-linear softening cohesive models), or *continuum approaches* (strain localization-based or regularized models) are used at the lower scale, the kinematic description of some, or both, scales cannot be considered smooth anymore, and the existence of the RVE can be questioned arguing that, in this case, the material loses the statistical homogeneity. A crucial consequence of this issue is the lack of objectivity of the results with respect to the size of the RVE. In (Nguyen et al., 2010) a recent attempt to overcome this flaw, for regularized non-local models, can be found.

This work is an attempt to address this issue in the setting of the Continuum Strong Discontinuity Approach (CSDA) to material failure, developed by the authors in the past (Oliver, 1995, Oliver et al., 2002). The essentials of the method are:

1. At the macroscopic level, material failure is captured via *strain-localization and finite elements with embedded regularized strong discontinuities.*
2. The microstructure of the smooth-strain part of the body is represented by a classical RVE, whose size is associated to standard statistic representativeness concepts.
3. A *failure-cell* at the microscopic scale, with the same size and topological properties than the RVE is associated to material points at the strain-localizing part of the microstructure. This failure-cell is enriched with appropriated material failure mechanisms with, apparently, no restriction on their type. Though, for the sake of simplicity, cohesive-bands with a predefined position have been used in this work, there is no "a priori" limitation on using more sophisticated material failure mechanisms,

e.g. arbitrarily propagating cracks or strong discontinuities (Oliver, 1995, Armero and Garikipati, 1996, Alfaiate et al., 2003). In contrast, this failure-cell is not claimed to be a RVE, in the sense of being statistically representative of any part of the macrostructure, although standard homogenization procedures are applied to it.

4. It is proven that homogenization of the RVE and failure-cell returns a macroscopic constitutive model (stress vs. strain) with the same format than classical inelastic-strain-based phenomenological models. A set of macroscopic inelastic-strain-like internal variables emerge naturally, whose evolution equation is ruled by the activation of material non-linearities and failure mechanisms at the failure-cell. In addition, a internal-length arises from that homogenization procedure, and it is naturally determined by the size of the chosen RVE and the amount of activated material failure mechanisms at the microstructure. This internal length is of the same order then the RVE and, determines the bandwidth of the macroscopic regularized strain-localization or displacement-discontinuity bands.
5. Based on this internal length, imported from the microstructure, the macrostructure is equipped with finite elements with embedded regularized strain-localization and displacement-discontinuities. Through this method, complete insensitivity of the structural response, with respect to the RVE size, and the macroscopic and microscopic finite element meshes is achieved, and material failure properties, like the fracture energy, are consistently up-scaled.

The mechanical derivation of the model is done in section 2, in section 3 the numerical aspects are presented and, in section 4, representative simulations are presented. Finally, section 5 is devoted to some concluding remarks.

2 MULTISCALE MODEL FOR FRACTURE

Let us consider the body $\mathcal{B}$, in Figure 1. At the macroscopic scale, the body is considered to exhibit strain-localization bands, with typical bandwidth h (very small in comparison with the dimensions of the macrostructure L, $h \ll L$), which, in turn, are h-regularizations of the discontinuities (cracks) observed at the macroscopic scale.

2.1 *Microscopic scale: RVE/failure cell*

We assume microstructures characterized by a RVE/failure-cell like that shown in Figure 2, having cohesive bands, $\mathcal{B}_{\mu,k}$, of very small thickness ($k << h_\mu$) where the dissipative processes can take place and strain localizes.

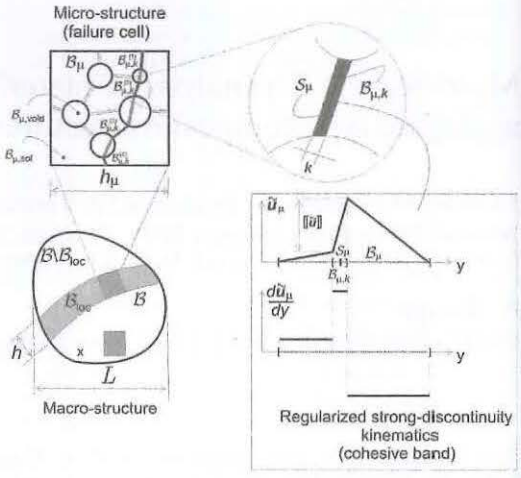

Figure 1. Multiscale failure model.

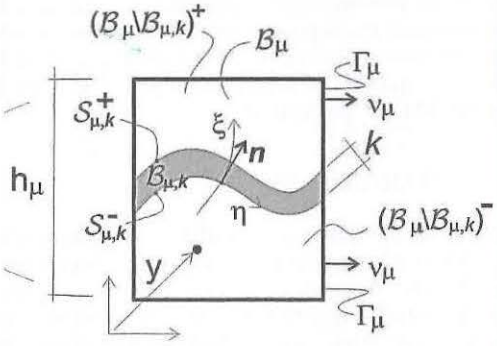

Figure 2. Multiscale model: Microstructure with cohesive bands.

2.1.1 *Kinematics: Microscopic strain field*

Without loss of generality, we are considering cohesive bands of constant width k. Thus, we define the band length $meas(\mathcal{S}_\mu) = \mathcal{B}_{\mu,k}/k$. Then, we assume that: $meas(\mathcal{B}_{\mu,k}) << meas(\mathcal{B}_\mu)$. In $\mathcal{B}_\mu$, we define the microscopic displacement:

$$\mathbf{u}_\mu(\mathbf{y}) = \mathbf{u}(\mathbf{x}) + \boldsymbol{\varepsilon}(\mathbf{x})\cdot\mathbf{y} + \tilde{\mathbf{u}}_\mu(\mathbf{y}) \tag{1}$$

where, $\mathbf{u}(\mathbf{x})$ and $\boldsymbol{\varepsilon}(\mathbf{x})$ are, respectively, the macroscopic displacement and strain of the point $\mathbf{x}$ in $\mathcal{B}$, respectively, and $\tilde{\mathbf{u}}_\mu$ is the microscopic displacement fluctuation that, for the cohesive bands is defined, in a local coordinate system (ξ,η) aligned with the band $\mathcal{B}_{\mu,k}$ (see Fig. 2), as follows:

$$\tilde{\mathbf{u}}(\xi,\eta) = \hat{\tilde{\mathbf{u}}}(\xi,\eta) + H_S^k(\xi)\boldsymbol{\beta}(\eta) \tag{2}$$

In equation (2), the displacement $\hat{\mathbf{u}}$ is a smooth field (see Fig. 3) whereas the second term of the RHS, is the k-regularized (k-ramp) function $H_S(\xi(\mathbf{y}))$ given by the expressions:

$$H_S(\xi(\mathbf{y})) = \begin{cases} 0 & \forall \quad \mathbf{y} \in (\mathcal{B}_\mu \setminus \mathcal{B}_{\mu,k})^- \\ 1 & \forall \quad \mathbf{y} \in (\mathcal{B}_\mu \setminus \mathcal{B}_{\mu,k}))^+; \\ \dfrac{\xi}{k} & \forall \quad \mathbf{y} \in \mathcal{B}_{\mu,k}) \end{cases} \tag{3}$$

$$\beta(\eta) \equiv \tilde{\mathbf{u}}_{\mathcal{B}_k^+}(\eta) - \tilde{\mathbf{u}}_{\mathcal{B}_k^-}(\eta).$$

where, $\beta(\eta)$ is the displacement jump across the cohesive band. A sketch of the displacement fluctuation field along ξ is displayed in Figure 3.

From equation (1), the micro strain $\boldsymbol{\varepsilon}_\mu$, assuming infinitesimal strain settings can be obtained as follows:

$$\boldsymbol{\varepsilon}_\mu(\mathbf{y}) = \nabla_{\mathbf{y}}^s \mathbf{u}_\mu = \boldsymbol{\varepsilon}(\mathbf{x}) + \tilde{\boldsymbol{\varepsilon}}_\mu(\mathbf{y}) = \boldsymbol{\varepsilon}(\mathbf{x}) + \nabla_{\mathbf{y}}^s \tilde{\mathbf{u}}_\mu(\mathbf{y}) \tag{4}$$

where $\tilde{\boldsymbol{\varepsilon}}_\mu$ is the micro strain fluctuation and supra-index $(\bullet)^s$ denotes the symmetric part of the corresponding tensor.

2.1.2 *Microscopic constitutive model*

The microstructure is considered constituted of a hardening material outside the cohesive bands, whereas this material exhibits strain-softening inside the bands. Then, the stress-strain relationship, in rate form, is given by:

$$\dot{\sigma}_\mu(\mathbf{y}) = \begin{cases} \mathcal{C}_\mu^{hard} : \dot{\boldsymbol{\varepsilon}}_\mu(\mathbf{y}); & \forall\, \mathbf{y} \in \mathcal{B}_\mu \setminus \mathcal{B}_{\mu,k} \quad (a) \\ \mathcal{C}_\mu^{soft} : \dot{\boldsymbol{\varepsilon}}_\mu(\mathbf{y}); & \forall\, \mathbf{y} \in \mathcal{B}_{\mu,k} \quad (b) \end{cases} \tag{5}$$

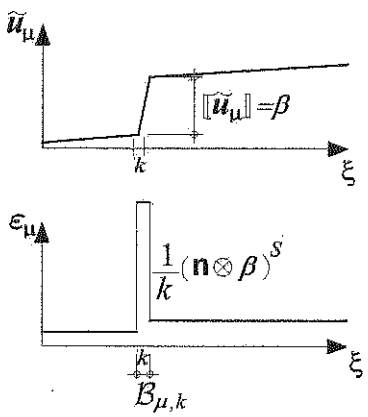

Figure 3. Multiscale model: Micro-displacement fluctuations and micro-strains at the cohesive band.

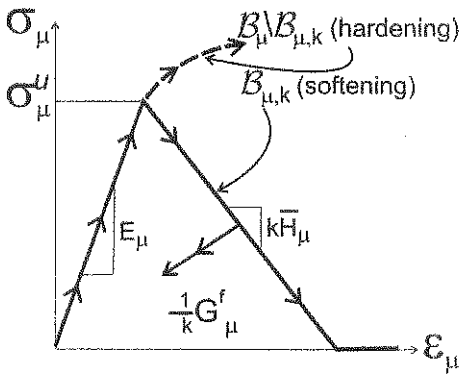

Figure 4. Constitutive model at the microstructure.

where σ_μ are the micro-stresses, and $\mathcal{C}_\mu^{hard}$ and $\mathcal{C}_\mu^{soft}$ are the microscopic tangent constitutive operators corresponding with the (rate) constitutive behavior at domains $\mathcal{B}_\mu \setminus \mathcal{B}_{\mu,k}$ and $\mathcal{B}_{\mu,k}$, respectively (see Fig. 4). At $\mathcal{B}_\mu \setminus \mathcal{B}_{\mu,k}$, $\mathcal{C}_\mu^{hard}$ corresponds with a strain-hardening constitutive behavior, so that no strain localization can take place. At $\mathcal{B}_k$, $\mathcal{C}_\mu^{soft}$ defines a strain-softening model which gives raise to strain localization. From the Continuum Strong Discontinuity Approach (CSDA) (Oliver and Huespe, 2004b, Oliver and Huespe, 2004a) it is well known that, as this strain localization takes place in the narrow bands of bandwidth k (the cohesive bands $\mathcal{B}_{\mu,k}$), regularization of the softening parameter as $H_\mu = k\bar{H}_\mu$; $\bar{H}_\mu = 1/2(\sigma_u^2)/(EG_\mu^f), G_\mu^f$ standing for the microscopic fracture energy (see Fig. 4), the continuum constitutive model in equation (5)-b, degenerates in an (implicit) traction-separation law, ruling the decohesion of the modeled discrete crack.

2.2 *Computational homogenization elements*

Computational homogenization is based on standard procedures lying on the strain homogenization concept and the Mandell-Hill principle (de Souza Neto and Feijóo, 2006) as described next.

2.2.1 *Strain homogenization: Minimal kinematic restrictions*

The strain homogeneity condition requires that[1]:

$$\boldsymbol{\varepsilon}(\mathbf{x}) = \frac{1}{\mathcal{B}_\mu} \int_{\mathcal{B}_\mu} \boldsymbol{\varepsilon}_\mu \, d\mathcal{B}_\mu \tag{6}$$

[1]From now on, and with some abuse of the notation, we will denote with the same symbol the *domain and its measure*, i.e.: $meas(\mathcal{B}_\mu) \equiv \mathcal{B}_\mu$.

and replacing (4) in (6), this equation results:

$$\boldsymbol{\varepsilon}(\mathbf{x}) = \boldsymbol{\varepsilon}(\mathbf{x}) + \frac{1}{\mathcal{B}_\mu}\int_{\mathcal{B}_\mu} \nabla^s \tilde{\mathbf{u}}_\mu \, d\mathcal{B}_\mu \tag{7}$$

which, in turn, yields:

$$\int_{\mathcal{B}_\mu} \nabla^s \tilde{\mathbf{u}}_\mu \, d\mathcal{B}_\mu = \int_{\Gamma_\mu} \left(\tilde{\mathbf{u}}_\mu \otimes^s \mathbf{v}_\mu\right) d\Gamma_\mu = \mathbf{0} \tag{8}$$

Thus, we define the space V_μ of kinematically admissible displacements fluctuations at the micro-scale, as being:

$$V_\mu := \left\{ \tilde{\mathbf{u}}_\mu \,|\, \int_{\Gamma_\mu} \left(\tilde{\mathbf{u}}_\mu \otimes^s \mathbf{v}_\mu\right) d\Gamma_\mu = \mathbf{0} \right\}. \tag{9}$$

Then, all micro displacement fluctuations: $\tilde{\mathbf{u}}_\mu \in V_\mu$ should be compatible with micro strain fluctuations satisfying the homogeneity condition.

2.2.2 *Hill-Mandel variational principle*

The Hill-Mandel principle equating the macroscopic point internal power and the average value of the microscopic internal power reads

$$\begin{aligned} \boldsymbol{\sigma}(\mathbf{x}) : \delta\boldsymbol{\varepsilon}(\mathbf{x}) &= \frac{1}{\mathcal{B}_\mu}\int_{\mathcal{B}_\mu} \boldsymbol{\sigma}(\mathbf{y}) : \delta\boldsymbol{\varepsilon}_\mu(\mathbf{y}) d\mathcal{B}_\mu \\ &= \frac{1}{\mathcal{B}_\mu}\int_{\mathcal{B}_\mu} \boldsymbol{\sigma}(\mathbf{y}) : \left(\delta\boldsymbol{\varepsilon}(\mathbf{x}) + \nabla^s_y \delta\tilde{\boldsymbol{u}}_\mu(\mathbf{y})\right) d\mathcal{B}_\mu \\ &\quad \forall\ \delta\boldsymbol{\varepsilon}, \delta\tilde{\boldsymbol{u}}_\mu \in V_\mu. \end{aligned} \tag{10}$$

Replacement of the appropriate values of $\delta\boldsymbol{\varepsilon}, \delta\tilde{\mathbf{u}}_\mu$ in equation (9) returns the classical strain homogenization principle

$$\sigma(\mathbf{x}) = \frac{1}{\mathcal{B}_\mu}\int_{\mathcal{B}_\mu} \sigma_\mu d\mathcal{B}_\mu. \tag{11}$$

which supplies the homogenized macro stresses, $\sigma(\mathbf{x})$, and the RVE virtual work principle (de Souza Neto and Feijóo, 2006)

$$\begin{aligned} &\int_{\mathcal{B}_\mu} \nabla^s \delta\tilde{\mathbf{u}}_\mu : \boldsymbol{\sigma}_\mu(\boldsymbol{\varepsilon} + \nabla^s_y \tilde{\mathbf{u}}_\mu) \, d\mathcal{B}_\mu = 0 \\ &\forall\ \delta\tilde{\mathbf{u}}_\mu \in V_\mu \end{aligned} \tag{12}$$

Equation (12) provides the solution for the micro-fluctuation field $\tilde{\mathbf{u}}_\mu$.

2.3 *Macroscopic scale: Homogenized constitutive model*

Substitution of the solution $\tilde{\mathbf{u}}_\mu(\mathbf{y}, \boldsymbol{\varepsilon})$ of equation (12) into equation (11) yields the macroscopic constitutive equation, whose rate form reads

$$\dot{\sigma}(\boldsymbol{\varepsilon}) = \frac{1}{\mathcal{B}_\mu}\int_{\mathcal{B}_\mu} \dot{\sigma}_\mu(\boldsymbol{\varepsilon} + \nabla^s_{\mathbf{y}} \tilde{\mathbf{u}}_\mu(\mathbf{y}, \boldsymbol{\varepsilon}) d\mathcal{B}_\mu. \tag{13}$$

Then, algebraic elaboration on equation (13), considering equations (4) and (5), yields the following *macroscopic homogenized constitutive model*

$$\dot{\sigma} = \mathcal{C}^{\,\mathrm{hom}} : \left(\dot{\boldsymbol{\varepsilon}}(\mathbf{x}) - \dot{\boldsymbol{\varepsilon}}^{(i)}\right) \tag{14}$$

where $\mathcal{C}^{\,\mathrm{hom}}$ is the macroscopic homogenized value of the hardening constitutive operator $\mathcal{C}_\mu^{hard}$ (de Souza Neto and Feijóo, 2006).

In equation (14) $\dot{\boldsymbol{\varepsilon}}^{(i)}$ are macroscopic internal variables, playing the role of inelastic strains, whose evolution is described in terms of the microstructural variables as

$$\dot{\boldsymbol{\varepsilon}}^{(i)} = \frac{1}{l_\mu}\zeta = \frac{1}{l_\mu}\overline{\left(\mathbf{n} \otimes^s \dot{\boldsymbol{\beta}}\right)}_{S_k} \tag{15}$$

i.e.: in terms of the activated failure mechanism and the band opening process at the microscale. In equation (15) notation $(\cdot)_{S_k}$ stands for the mean value of (.) along the microscopic activated failure mechanism, i.e.:

$$\overline{\left(\mathbf{n} \otimes^s \dot{\boldsymbol{\beta}}\right)}^S_{S_k} = \frac{1}{S_k}\int_{S_k} \left(\mathbf{n} \otimes^s \dot{\boldsymbol{\beta}}\right)^S dS \tag{16}$$

In addition, the evolution equation (15) incorporates the microscale length l_μ, defined as:

$$l_\mu = \frac{\mathcal{B}_\mu}{S_k} = \mathcal{O}(h_\mu) \tag{17}$$

In summary, in the context of the description of complex materials equipped with morphological descriptors (Oliver et al., 2012, Huespe et al., 2013) equations (14) to (17) retrieve a *constitutive equation equipped with an internal length and with internal variables described by the microstructure behavior.*

3 NUMERICAL ASPECTS: FINITE ELEMENT MODEL

The multiscale formulation described above is implemented by means of a finite element model following the outlines given by the FE² technology

(Özdemir et al., 2008). Accordingly, two finite element models are used, one for the macroscopic structure and another for the microstructure through a discretized RVE/failure-cell.

3.1 *RVE/failure-cell finite element model*

Standard quadrilateral finite elements are adopted for the numerical simulation of the RVE/failure-cell response. The cohesive bands, $\mathcal{B}_{k,\mu}$, are also modeled by quads of very small thickness ($k \ll h_\mu$) as shown in Figure 5. They are equipped with the constitutive models defined in Figure 4 and equation (5), so that only elements on the cohesive band can exhibit strain localization. The model is solved according with the RVE virtual work principle in equation (12).

Notice that the driving force (external action) for the equation solution is the macroscopic strain $\boldsymbol{\varepsilon}$ and no external force is explicitly applied.

The corresponding non-linear problem in the RVE/failure-cell is then solved for the micro-displacements fluctuation discretized as

$$\tilde{\mathbf{u}}_\mu(\mathbf{y},\boldsymbol{\varepsilon}) = \sum_{1}^{nnode} N_i(\mathbf{y})\mathbf{d}_{\mu,i}(\boldsymbol{\varepsilon}) \qquad (18)$$

where $N_i(\mathbf{y})$ are the standard interpolation functions for quadrilaterals and $\mathbf{d}_{\mu,i}$ are the nodal values. Dirichlet boundary conditions precluding the rigid body motions and, in addition, the minimal boundary restriction in equations (9) are also imposed.

Then, material failure propagates naturally, as the softening behavior and, therefore, strain localization, is incepted in the finite elements defining the cohesive bands. At every time step of the analysis, those elements who are in in-loading state, define the active set of cohesive bands $\mathcal{B}_{\mu,k}$ (see Fig. 5) or the *active failure mechanism.*

3.2 *Finite element model at the macro-structure: Material failure propagation*

At the macroscopic scale, propagation of material failure is modeled using the *crack path field* and *strain injection* techniques recently developed by the authors (Oliver et al., 2014). They are based on using goal oriented assumed-strain fields injected in selected domains, via mixed formulations.

- In a ***first injection stage,*** embedded localization bands, of bandwidth l_μ, are incrementally injected (prior to development of displacement discontinuities) in an evolving subdomain of the macro-structure, $\mathcal{B}_{loc}$ (see Fig. 6) were both the material discontinuous bifurcation (Willam and Sobh, 1987) an the in-loading conditions are fulfilled.
- These embedded localization bands have an isotropic character (there is no preferred direction in them), but exhibit extremely good ability to propagate material failure in the right material directions. Therefore, its evolving position and intensity is used to determine a scalar field (the crack propagation field) whose zero level set constitutes a reliable approximation to the actual crack path.
- In a ***second injection stage,*** the obtained crack path field, S (see Fig. 6) is used to determine the correct position of an elemental embedded strong-discontinuity strain field, which is incrementally injected in the set of elements, $\mathcal{B}_{dis}$ (see Fig. 6).

The resulting procedure is a robust and efficient technique to model propagating material failure in a finite element discretized body. Its intra-elemental character (one-element bandwidth band captures the regularized strain-localization) makes it especially appropriate for capturing material failure propagation in coarse meshes, in contraposition of the alternative extra elemental character techniques (e.g. phase field models) for capturing propagating material failure, where several elements have to span the localization band, this leading to, some-times un-affordably fine finite element meshes (B. Bourdin et al., 2000, Miehe et al., 2010). In addition, its implementation in an existing finite element code has a little invasive character.

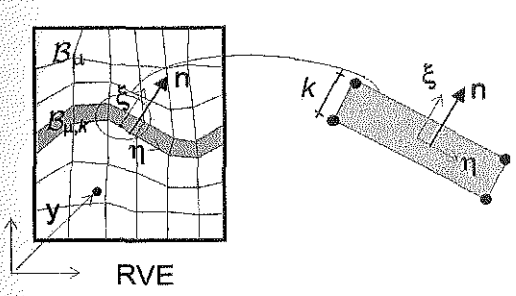

Figure 5. Micro-scale numerical model.

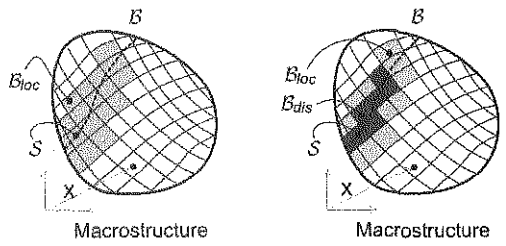

Figure 6. Strain injection procedures. Left: embedded strain localization bands injection in $\mathcal{B}_{loc}$. Right: embedded strong discontinuity injection in $\mathcal{B}_{dis}$.

4 REPRESENTATIVE SIMULATIONS: TWO-SCALE MODELING OF FAILURE PROPAGATION IN A CONCRETE-LIKE MATERIAL

In order to explore the potential of the proposed formulation, numerical experimentation is performed on the basis of a material whose mesostructure mimics the cement-aggregate composition of concrete. This is not an attempt to obtain quantitative results, to fit some specific experiment, but, rather, to evaluate the potential of multiscale modeling, incorporating the microstructure morphology, in simulation of *complex macroscopic behavior using simple microscopic/mesoscopic models*. It should be mentioned that, unlike what is regularly done in the literature, the issue tackled here is not only modeling the macroscopic homogenized behavior at a single point of the macrostructure, but, also, *the full macroscopic structural behavior, including material failure onset and propagation* and obtaining a *complete action/response behavior during the structural failure*.

The strip in Figure 7, incorporating a central opening to break the inhomogeneity, is subjected to horizontal stretching, induced by a constant displacement, Δ, under the action of the external force **F**.

The mesostructure morphology is sketched by the failure-cell of Figure 8 roughly characterized by some cylindrical aggregates of different sizes, immersed in a matrix of mortar. Grains and matrix are numerically modeled by quadrilateral finite elements. Additionally, the failure cell is equipped with a number of, very narrow, cohesive bands; some of them surrounding the aggregates (thus its failure representing possible aggregate/mortar decohesion) and some others crossing the matrix and connecting grains (its failure corresponding to mortar cracks).

Their activation allows modeling a number of failure mechanisms: those excluding the interior of the aggregates i.e.: *extra-granular failure mechanisms* or those including the grains breakage i.e.: *intra-granular failure mechanisms*.

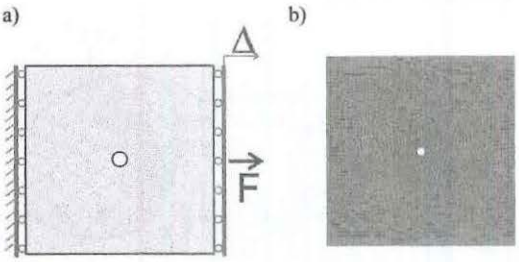

Figure 7. Strip with central opening under uniaxial stretching: a) macroscopic (structural) geometry. Dimensions (1 m × 1 m). b) Finite element mesh (quadrilaterals).

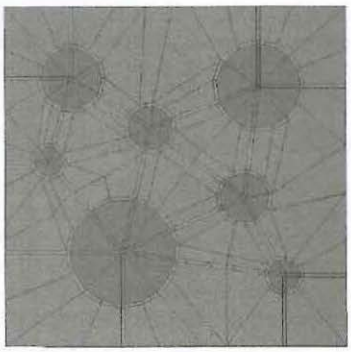

Figure 8. Strip with central opening under uniaxial stretching. 2D microscopic failure cell incorporating: a) cylindrical-shaped aggregates, immersed in a matrix and b) intra-granular, extra-granular and grain-matrix cohesive bands. Dimensions (1 mm × 1 mm).

Constitutive behavior at the matrix is assumed to be elastic; at the cohesive bands it is assumed to be ruled by a very simple model: the *only-tension-failure* constitutive model developed by the authors in the past (Oliver et al., 1990) that precludes inelastic behavior in pure compression stress states (see Fig. 9).

Then, three different types of concrete are analyzed, using the mesostructure in Figure 8, equipped with different material properties, i.e.:

- Regular-Weight-Aggregate (RWA) concrete: properties of matrix and aggregates are taken as those typically described in the literature for standard concrete.
- Light-Weight-Aggregate (LWA) concrete: properties of aggregates are taken as those typically described in the literature for light (ceramic) aggregates.
- Medium-Weight-Aggregate (MWA) concrete: aggregate properties are taken in between the other two cases.

The goal of the experiments is to observe how, for the same experiment, the mechanical properties of the aggregates affect the mesoscopic failure mechanism and, in turn, the macroscopic structural response.

4.1 *Regular Weight Aggregate (RWA) concrete modeling*

The mesostructure in Figure 8 is equipped with the material properties displayed in Table 1.

In Figure 10, qualitative results at the macroscopic level are presented.

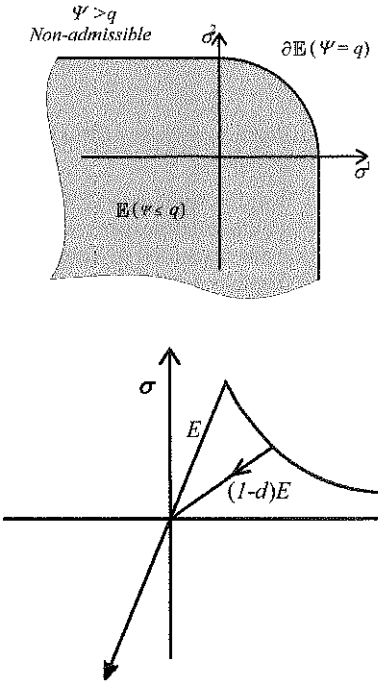

Figure 9. Only-tension-failure continuum damage model: a) elastic domain in the 2D principal stress, $\sigma^{(1)} - \sigma^{(2)}$, space, b) resulting uniaxial stress-strain constitutive model.

Table 1. Regular Weight Aggregate (RWA) concrete. Material properties at the mesoscopic level.

	Young modulus (E)	Poisson ratio (ν)	Ultimate stress (σ_u)	Fracture energy (G_μ^f)
Mortar (bulk)	20 Gpa	0.2	(Elastic)	(Elastic)
Mortar (cohesive bands)	20 Gpa	0.2	3.0 Mpa	700 J/m^2
Aggregates (bulk)	100 Gpa	0.2	(Elastic)	(Elastic)
Aggregates (cohesive bands)	100 Gpa	0.2	15.0 Mpa	3500 J/m^2

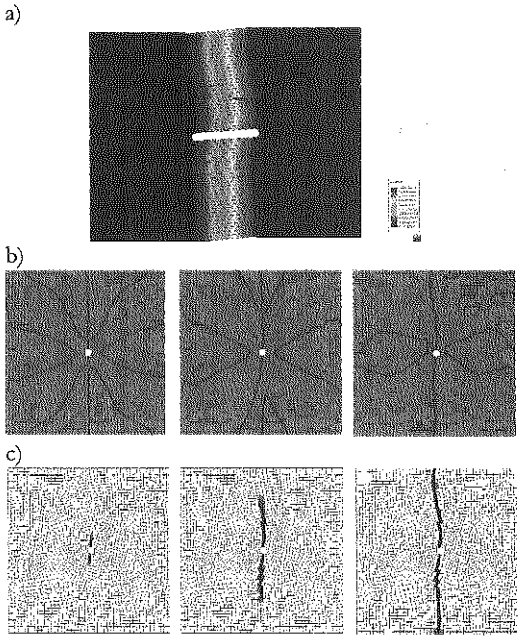

Figure 10. *Regular Weight Aggregate (RWA) concrete. Macroscopic results.* a) Deformed (amplified) shape showing the contours of horizontal displacements. b) Evolution, at sequential stages of the analysis, of the captured crack-path field. c) Evolution, at sequential stages of the analysis, of the strain injection pattern (darker zones correspond to strain-injected elements).

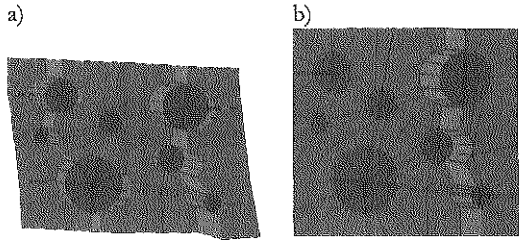

Figure 11. *Regular Weight Aggregate (RWA) concrete. Mesoscopic results.* Deformation of a typical failure cell displaying the failure modes: a) at the initiation of the macroscopic localization (amplification factor = 1000), b) at the end of the loading process (amplification factor = 200).

Those results show a macroscopic, approximately vertical, crack starting at the opening and exhibiting a mixed Mode I failure.

At the mesoscopic level, results for the deformation (fluctuations) of a typical failure-cell (nearby the opening in the macroscopic failure path) can be seen, conveniently amplified, in Figure 11. There it can be checked that, at an initial stage of the macroscopic localization, the failure-cell displays several (very small in amplitude) competing failure mechanisms (Fig. 11-a)). Later on, an *extragranular failure mechanism,* involving aggregate/

matrix decohesion and mortar cracking, prevails (Fig. 11-b)), characterizing the mesoscopic failure for this type of concrete.

In Figure 12 the evolution of the macroscopic energy along the process is presented. It can be noticed that the numerically observed dissipated energy computed as

$$E^{numerical} = \int_{t=0}^{t=\infty} F(t) \cdot \dot{\Delta}(t) dt \tag{19}$$

where F and Δ are defined in Fig. 7-a), see also Fig. 16) matches very well the theoretical value computed as:

$$E^{theoretical} = L_{macro} G^f_{macro}$$
$$G^f_{macro} \equiv \overline{\left(G^f_\mu\right)}_{S_\mu} = \frac{1}{S_\mu} \int_{S_\mu} G^f_\mu(\mathbf{y}) dS \tag{20}$$

i.e.: the length of the macroscopic crack, L_{macro}, times the macroscopic fracture energy G^f_{macro}. The theoretical value of G^f_{macro} is computed as the average, along the mesoscopic failure-cell failure path in Fig. 11-b), of the mesoscopic fracture energy (G^f_μ in Table 1).

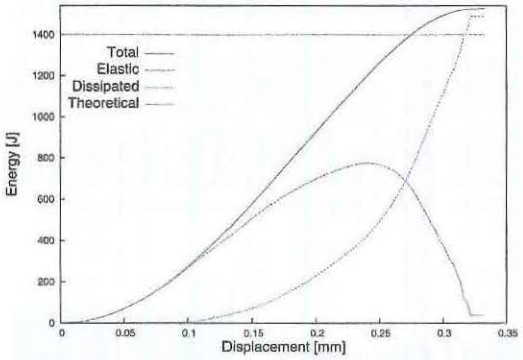

Figure 12. *Regular Weight Aggregate (RWA) concrete.* Numerically computed energy/dissipation evolution curves.

Table 2. Light Weight Aggregate (LWA) concrete. Material properties at the mesoscopic level.

	Young modulus (E)	Poisson ratio (ν)	Ultimate stress (σ_u)	Fracture energy (G^f_μ)
Mortar (bulk)	28.6 Gpa	0.2	(Elastic)	(Elastic)
Mortar (cohesive bands)	28.6 Gpa	0.2	3.0 Mpa	700 J/m^2
Aggregates (bulk)	6.8 Gpa	0.2	(Elastic)	(Elastic)
Aggregates (cohesive bands)	6.8 Gpa	0.2	0.7 Mpa	166 J/m^2

4.2 *Light Weight Aggregate (LWA) concrete modeling*

Now, Light Weight Aggregate (LWA) concrete is considered. The material properties, for a ceramic-type aggregate are presented in Table 2.

Figure 13 displays a macroscopic failure mechanism fairly similar to the one in the previous (RWA) case.

However the mesoscopic failure mechanism is substantially different: the activated mechanism goes through the aggregates (see Fig. 14-b), thus defining an intra-*granular failure mechanism.*

As for the energy dissipation, in Figure 15 good agreement of the theoretical energy dissipation and the numerical one (computed according equation (19), see also Fig. 16) is shown.

Notice that the energy dissipation of the process for this LWA concrete (850 J) is smaller than the one for NWA concrete in Figure 12 (1500 J). This is due to the fact that, in the present case, the mesoscopic failure mechanism, in Fig. 14-b), crosses the (weaker) aggregates, which are endowed with a lower fracture energy (check G^f_μ in Table 2 versus Table 1). Therefore the macroscopic fracture energy, G^f_{macro}, in equation (20) is smaller.

4.3 *Medium Weight Aggregate (MWA) concrete modeling*

As an intermediate case, the numerical experiment is repeated with the material properties presented in Table 3.

The macroscopic and mesoscopic failure mechanisms (not displayed) are similar to the ones, in Figure 10 and Figure 11, for RWA concrete. However, even if the qualitative effects of the different mesoscopic properties are not relevant, the quantitative structural response is very affected as it will be shown in next paragraph.

4.4 *Structural response*

Quantitative responses are now measured in terms of the force-displacement evolution curves, F –Δ in Figure 7-a), as shown in Figure 16.

There it can be observed that:

- RWA concrete (regular concrete) behaves as observed in normal plain concrete. After an

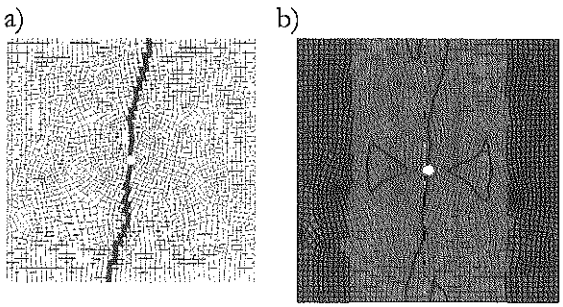

Figure 13. *Light-Weight-Aggregate (LWA) concrete. Macroscopic results.* a) strain injection pattern (darker zones correspond to strain-injected elements) at the end of the loading process, b) captured crack-path field.

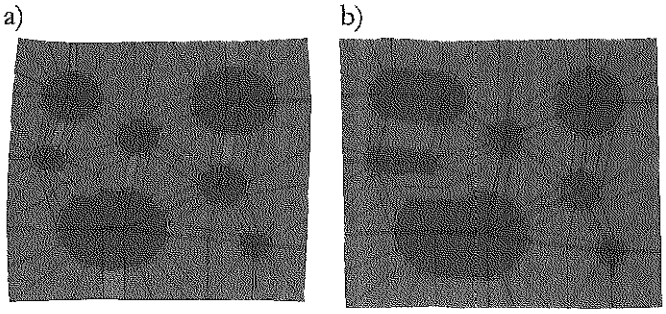

Figure 14. Light-Weight Aggregate (LWA) concrete. Mesoscopic results. Deformation of a typical failure cell displaying the failure modes: a) at the initiation of the macroscopic localization (amplification factor = 1000), b) at the end of the loading process (amplification factor = 200).

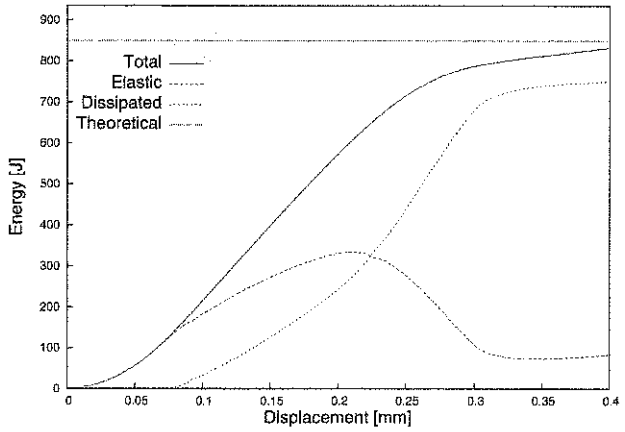

Figure 15. *Light-Weight Aggregate (LWA) concrete.* Numerically computed energy/dissipation evolution curves.

initial elastic branch, the structure exhibits some inelastic hardening and then fails abruptly (brittle failure).

- Introduction of light aggregate (MWA, LWA) concrete translates into substantial loss of the maximum carrying capacity but, also, in a more ductile failure: the non-linear hardening branch disappears and, immediately after the elastic branch, the structure softens in a smoother manner (ductile failure).

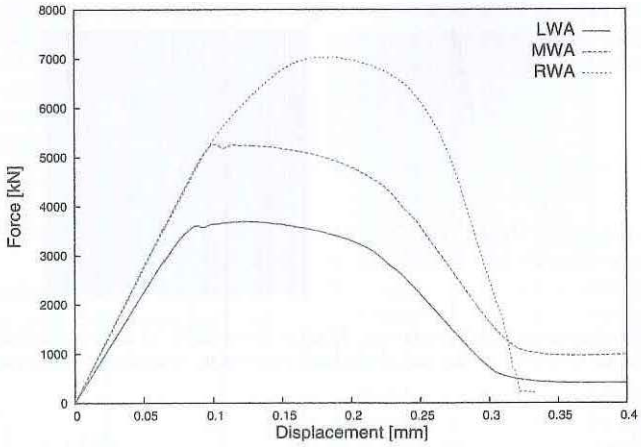

Figure 16. Structural, F – Δ, responses for the three considered types of concrete. Regular Weight Aggregate (RWA) concrete, Light Weight Aggregate (LWA) concrete and medium Weight Aggregate (MWA) concrete.

Table 3. Medium Weight Aggregate (MWA) concrete. Material properties at the mesoscopic level.

	Young modulus (E)	Poisson ratio (ν)	Ultimate stress (σ_u)	Fracture energy (G_μ^f)
Mortar (bulk)	28.6 Gpa	0.2	(Elastic)	(Elastic)
Mortar (cohesive bands)	28.6 Gpa	0.2	3.0 Mpa	700 J/m^2
Aggregates (bulk)	19.9 Gpa	0.2	(Elastic)	(Elastic)
Aggregates (cohesive bands)	19.9 Gpa	0.2	2.1 Mpa	487 J/m^2

Both observations coincide with the expectations for this types of concrete.

5 CONCLUDING REMARKS

Along this work, multiscale (FE^2) techniques have been used to model material failure of concrete-like materials.

A computational homogenization setting has been proposed which, keeping the essentials of classical computational homogenization techniques, naturally introduces a length scale, related to the RVE size and the mesoscale failure mechanism, into the induced macroscopic homogenized model. This microscopic length scale can be interpreted as the actual width of the fracture process zone, defining the bandwidth of the macroscopic localization band that captures the crack at the structural level. It has been frequently claimed in modeling of concrete materials (Bazant and Jirásek, 2002) and it is automatically retrieved here through the homogenization process.

At the macroscopic scale, this microscopic length scale is locally used in the context of the Continuum Strong Discontinuity Approach to material failure (Oliver and Huespe, 2004a), and introduced, as a regularization parameter, into a new technique (Oliver et al., 2014) for capturing the macroscopic propagation of cracks by means of finite elements with embedded discontinuities.

The result is a multiscale approach, that preserves the correct dissipation and objectivity, with respect both the macroscopic size of the finite element mesh and the size of the failure cell, which, in turn, can be readily connected with recent proposals for similar purposes (Sánchez et al., 2013).

Finally, the proposed techniques have been applied to modeling concrete like materials (i.e., materials that, at the mesoscopic level, are constituted by aggregates and mortar). Although the complexity of the mesoscale morphology is very limited by the computational cost of the combined multiscale computations, the potential of the approach is clearly stated by the presented examples.

ACKNOWLEDGMENT

The research leading to these results has received funding from the European Research Council under the European Union's Seventh Framework

Programme (FP/2007–2013)/ERC Grant Agreement n. 320815, Advanced Grant Project COMPDES-MAT.

REFERENCES

Alfaiate, J., Simone, A. & Sluys, L.J. 2003. Non-homogeneous displacement jumps in strong embedded discontinuities. *International Journal of Solids and Structures,* 40, 5799–5817.

Armero, F. & Garikipati, K. 1996. An analysis of strong discontinuities in multiplicative finite strain plasticity and their relation with the numerical simulation of strain localization in solids. *Int.J. Solids and Structures,* 33, 2863–2885.

Bazant, Z.P. & Jirásek, M. 2002. Nonlocal Integral Formulations of Plasticity and Damage: Survey of Progress. *Journal of Engineering Mechanics,* 1119, 1125:1149.

Bourdin B., Francfort, G.A. & J-J. Marigo 2000. Numerical experiments in revisited brittle fracture. *Journal of the Mechanics and Physics of Solids,* 48, 797–826.

De Souza Neto, E.A. & Feijóo, R.A. 2006. Variational foundations of multi-scale constitutive models of solid: small and large strain kinematical formulation. *LNCC Research & Development Report,* 16.

Huespe, A., Oliver, J. & Mora, D. 2013. Computational modeling of high performance steel fiber reinforced concrete using a micromorphic approach. *Computational Mechanics,* 1–22.

Miehe, C., Welschinger, F. & Hofacker, M. 2010. Thermodynamically consistent phase-field models of fracture: Variational principles and multi-field FE implementations. *Int. J. Numer. Meth. Engng.,* 83.

Nguyen, V.P., Lloberas-Valls, O., Stroeven, M. & Sluys, L.J. 2010. On the existence of representative volumes for softening quasi-brittle materials-a failure zone averaging scheme. *Computer Methods in Applied Mechanics and Engineering.*

Oliver, J. 1995. Continuum modelling of strong discontinuities in solid mechanics using damage models. *Computational Mechanics,* 17, 49–61.

Oliver, J., Cervera, M., Oller, S. & Lubliner, J. Isotropic damage models and smeared crack analysis of concrete. *In:* AL., N.B.E., ed. Proc. SCI-C Computer Aided Analysis and Design of Concrete Structures, 1990. 945–957.

Oliver, J. & Huespe, A.E. 2004a. Continuum approach to material failure in strong discontinuity settings. *Computer Methods in Applied Mechanics and Engineering,* 193, 3195–3220.

Oliver, J. & Huespe, A.E. 2004b. Theoretical and computational issues in modelling material failure in strong discontinuity scenarios. *Computer Methods in Applied Mechanics and Engineering,* 193, 2987–3014.

Oliver, J., Huespe, A.E. & Dias, I.F. 2014. Crack-path field and strain-injection techniques in computational modeling of propagating material failure. *Comp. Meth. in Appl. Mech. and Eng.,* Submitted.

Oliver, J., Huespe, A.E., Pulido, M.D.G. & Chaves, E. 2002. From continuum mechanics to fracture mechanics: the strong discontinuity approach. *Engineering Fracture Mechanics,* 69, 113–136.

Oliver, J., Mora, D., Huespe, A. & Weyler, R. 2012. A micromorphic model for steel fiber reinforced concrete. *International Journal of Solids and Structures,* 49, 2990–3007.

Özdemir, I., Brekelmans, W. & Geers, M. 2008. FE2 computational homogenization for the thermo-mechanical analysis of heterogeneous solids. *Computer Methods in Applied Mechanics and Engineering,* 198, 602–613.

Sánchez, P.J., Blanco, P.J., Huespe, A.E. & Feijóo, R.A. 2013. Failure-Oriented Multi-scale Variational Formulation: Micro-structures with nucleation and evolution of softening bands. *Comput. Methods Appl. Mech. Engrg.,* 257, 221–247.

Willam, K. & Sobh, N. 1987. Bifurcation analysis of tangential material operators. *In:* Pande, G.N. & Middleton, J. (eds.) *Transient/Dynamic Analysis and Constitutive Laws for Engineering Materials.* Martinus-Nijhoff Publishers.